36. D. G. Scheliecher, C. Eberhardy, *IAU Circular* **7455** (2000); personal communication (2001).
37. Although it is based on the overly simplified Wegmann model (*11*), a good discussion of how to interpret the x-ray spectra for variable solar wind flux and composition is given by N. A. Schwadron and T. E. Cravens [*Astrophys. J.* **544**, 558 (2000)].
38. We have used the cometary ephemerides (DE-405, mid-June 2000, epoch = 4 August 2000) of D. K. Yeomans *et al.* found at http://ssd.jpl.nasa.gov/horizons.html to target the comet and to remap our observations into a comet-centered reference frame. The estimated pointing uncertainties for the CXO and EUVE spacecraft are 1″ and 10″, respectively. The estimated ephemeris uncertainties for C/LINEAR are large, due to the large nongravitational (i.e., jet) forces created during the comet's prolonged breakup in July 2000, on the order of 10″ or so, and along with the 1′ HEW of the EUVE scanner telescopes, dominate the EUVE positional uncertainties of our observations. For the CXO observations, the limited number of detected photons (~13,000) restricted the effective detector resolution, due to statistical counting uncertainties, to pixels of 10″ extent.
39. E. Feigelson *et al.*, *Bull. Am. Astron. Soc.* **32**, 27.02 (2000), http://www.aas.org/publications/baas/v32n3/head2001/173.htm
40. The SOHO and WIND data were graciously provided by R. Lepping of NASA/Goddard Spaceflight Center and H. Ogawa of University of Southern California. The ACE data were provided courtesy of S. Nyland of Johns Hopkins University. We are grateful for the cometary ephemeredes of D. K. Yeomans *et al.*, found at the Jet Propulsion Laboratory Horizons website used to reduce our data. The optical images and photometry of C/LINEAR on 14 July 2000 was provided by H. Mikuz of the Crni Vrh Observatory, Slovenia. We thank the Chandra X-ray Center, especially R. Hain for reconstructing the comet images, and B. Stroozas and the EUVE Science Operations team for working with us to schedule the moving target observations. C.M.L. was supported in part by NASA Planetary Astronomy Program Grant No. NAGW188 and by observing grants NAG5-6141 and NAG5-6155. K.D. gratefully acknowledges support from the German Bundesministerium für Bildung, Wissenschaft, Forschung und Technologie (BMBF/DARA) and the Max-Planck-Gesellschaft. S.J.W. was supported by NASA contract NAS8-39073.

26 December 2000; accepted 24 April 2001

# Imaging and Photometry of Comet C/1999 S4 (LINEAR) Before Perihelion and After Breakup

**Tony L. Farnham,[1]* David G. Schleicher,[2] Laura M. Woodney,[2] Peter V. Birch,[3] Clara A. Eberhardy,[4] Lorenza Levy[5]**

**We analyzed photometric measurements and images of comet C/LINEAR before perihelion and after its breakup. Results from our photometry data include a lower limit of 0.44 kilometer for the radius of the nucleus before breakup, and a determination that it was depleted in carbon-chain molecules relative to most other comets. Our imaging and modeling results, which include a constraint on the rotational state of the nucleus, indicate that the disintegration likely started on 18 or 19 July 2000. The total mass detectable in the dust tail after the breakup was $3 \times 10^8$ kilograms, comparable to one of the fragments in the Hubble Space Telescope images; we therefore infer that most of the comet's original mass is hidden in remnants between 1 millimeter and 50 meters in diameter.**

Comet C/1999 S4 (LINEAR) passed its closest point to Earth, 0.364 AU, on 23 July 2000, 3 days before it reached perihelion. Coincidentally, the comet completely disintegrated within a few days of its closest approach to Earth. The timing of this event was ideal because astronomers taking advantage of the favorable geometric conditions to observe C/LINEAR were able to obtain measurements of the spontaneous disintegration of its nucleus. These measurements, combined with observations before and after the disruption, constitute a unique data set that can be used to investigate the structure and composition of the comet's nucleus as well as the processes contributing to the breakup. We observed C/LINEAR for 14 nights with narrowband photometry and obtained charge-coupled device (CCD) images on 36 nights.

Our photometric observations began on 5 December 1999, when the comet was 3.57 AU from the Sun, and concluded on 1 August 2000, about 1 week after the comet's disintegration (Table 1). Data were obtained using a photoelectric photometer equipped with pulse-counting electronics with the 72-inch (1.8-m) Perkins and 42-inch (1.1-m) Hall telescopes at Lowell Observatory. Emission bands of OH, NH, CN, $C_2$, and $C_3$ were isolated with narrowband filters, and the reflected continuum was evaluated by measurements of dust grains at wavelengths of 345, 445, and 526 nm (*1*). Standard procedures were followed in data acquisition, reduction, and computation of gas ($Q$) and dust-equivalent [$A(\theta)f\rho$] production rates (*2, 3*).

The heliocentric distance ($r_H$) dependences of the derived production rates for the individual observations are given in Fig. 1; mean production rates for each night are shown in Table 1. CN, the best-measured gas species, exhibited the expected increase in $Q$ as $r_H$ decreased from 3.56 to 2.18 AU, before leveling or slightly dropping between 1.15 and 0.80 AU. As originally reported (*4*), the three consecutive nights in June show considerable variability, with all gas species peaking on 11 June with values more than 40% greater than on the surrounding nights. This minor outburst, confirmed by monitoring data from the Solar Wind Anisotropies (SWAN) instrument onboard the Solar and Heliospheric Observatory (SOHO) (*5, 6*), was one of a series of sporadic outbursts or partial fragmentations that preceded the disintegration of the comet. The SOHO record also indicates that our 13 July measurements were obtained shortly after a minor outburst, so they should be near the baseline level of comet activity. Therefore, we fit a quadratic function to the CN data (Fig. 1), excluding the 11 June outburst and the late July data taken after the breakup of the nucleus. For comparison, we then transposed the CN production curve to the plots of the other species in Fig. 1 (*7*).

The transposed CN curves are consistent with the measured $Q$ values of OH and $C_2$ at large $r_H$, with CN and $C_2$ increasing by a factor of ~18 between December 1999 and July 2000 while OH increased by a factor of 28. In contrast, the derived dust production increased by less than a factor of 3 during the apparition and was essentially constant as $r_H$ decreased from 3.56 to 2.18 AU, an interval in which the gas production increased by a factor of 6. These characteristics of the dust imply that the measured values of $A(\theta)f\rho$ at $r_H > 2$ AU were not true measures of ongoing dust production, but rather were dominated by dust that was released before C/LINEAR's discovery and remained in the comet's coma as a result of the combination of low outflow velocity and small radiation pressure at large $r_H$. This scenario is consistent with that expected for a dynamically new comet (*8*), which typically exhibits excessive activity at $r_H > 5$ AU and then brightens more slowly as this activity declines (*9*). As a

[1]Department of Astronomy, University of Texas, Austin, TX 78712, USA. [2]Lowell Observatory, 1400 West Mars Hill Road, Flagstaff, AZ 86001, USA. [3]Perth Observatory, Walnut Road, Bickley 6076, Western Australia. [4]Department of Astronomy, University of Washington, Physics/Astronomy Building, Stevens Way, Box 351580, Seattle, WA 98195, USA. [5]Department of Physics and Astronomy, Northern Arizona University, Box 6010, Flagstaff, AZ 86011, USA.

*To whom correspondence should be addressed. E-mail: farnham@astro.as.utexas.edu

consequence, we assume that only the June and early July observations of the dust are useful in deriving the quasi-instantaneous dust-to-gas ratio, as measured by $\log[A(\theta)f\rho/Q(\mathrm{OH})]$, whose value of $\sim -25.6$ is in the mid-range for comets (*10*). Finally, dust grains throughout the apparition are measured as slightly reddened, by about 10% per 100 nm, a typical value for cometary dust (*11*).

On the basis of our OH production rates, total water production rates can be determined (Table 1) and used to derive the surface area required to vaporize this much water ice (*12*). The 13 July data are consistent with an active area of 2.4 km$^2$ but may be slightly elevated after the minor outburst. A month earlier, on 12 June, an area of about 5 km$^2$ is required; however, this larger value may be affected by residual gas from the outburst 1 day earlier. In comparison, the observations early in the apparition ($r_H > 2$ AU) imply an active area of 3 to 4 km$^2$. Overall, a comparison of the baseline activity, as indicated by the quadratic curve, with the water vaporization model (*12*) implies a slowly decreasing active area throughout the apparition. This is supported by the SWAN/SOHO measurements from late May to 18 July (*6*), in which the baseline active area drops by nearly 50% (*13*). This may be due to the depletion of volatiles in the surface layer of the comet's nucleus (*14*). Our smallest derived active area of 2.4 km$^2$ provides a lower limit on the surface area of the nucleus, which in turn corresponds to a minimum effective radius of 0.44 km. If the comet was approaching the Sun for the first time, one might expect that the entire surface was active, rather than being crusted over, and so the actual radius might have been near this minimum value.

Relative abundances of the minor gas species, based on the production rate ratios, reveal a $C_2$/CN ratio about one-half the typical value (*10, 15*). This places C/LINEAR in the taxonomic class of carbon chain–depleted comets (*10*). Although 9 of 18 Jupiter-family comets within the restricted database were depleted (*10*), only 3 of 23 non–Jupiter-family comets showed this depletion, and none of these three were dynamically new. If this ratio is primordial (*10*), then the depletion might imply that C/LINEAR first originated in the Kuiper Belt and was then gravitationally scattered, probably by Neptune, into the Oort Cloud (*16*). C/LINEAR was also depleted in CO, methane, methanol, and ethane (*5, 17, 18*); however, these depletions are interpreted as evidence that C/LINEAR formed in the Jupiter-Saturn regime (*18*).

From 2 November 1999 to 9 July 2000, we obtained 28 nights of CCD images from the Lowell and McDonald observatories (*1, 19*). Inspection of a representative sample of images obtained between November 1999 and March 2000 (when C/LINEAR entered solar conjunction) reveals no unusual features in the coma or tail. After it left solar conjunction in May, however, C/LINEAR had changed markedly, frequently displaying unusual morphology in its inner coma (Fig. 2) and experiencing a number of outburst events.

Observations from 5 July show that C/LINEAR was in an outburst stage, ultimately brightening by more than 1.5 magnitudes (in a 3-arc sec radius aperture) on 6 July before fading again. The coma morphology during and after this outburst showed several interesting features: a pair of symmetric "wings" that persisted for 3 days, a plume of material 5000 km long (*20*) oriented along one of the wings, and a coma that elongated with time (Fig. 2). Interestingly, the coma in the sunward direction was essentially unaffected by the outburst, maintaining the same basic shape and brightness throughout. In Hubble Space Telescope (HST) images from 7 July, a small fragment is seen moving down the tail (*5, 21*), suggesting that

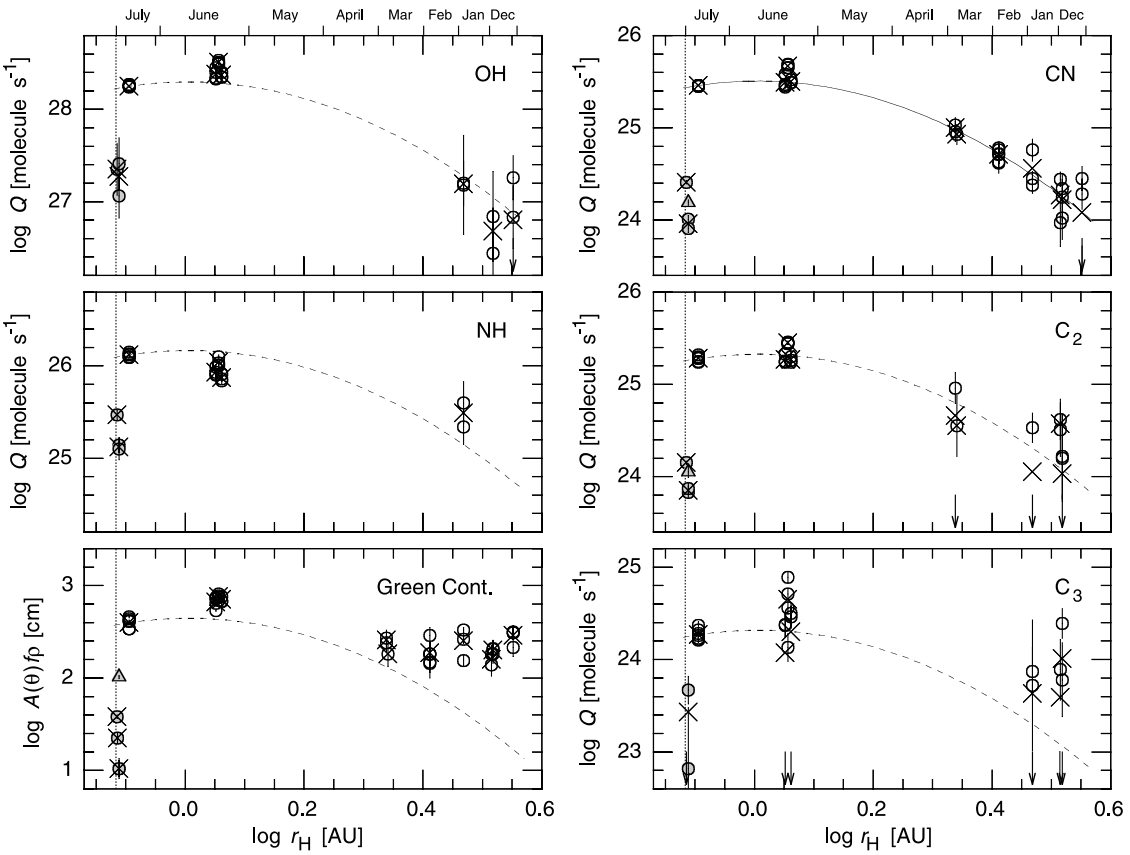


**Fig. 1.** Production rates as a function of heliocentric distance for C/LINEAR. Observations obtained before perihelion (open symbols) and after the comet's breakup (shaded symbols) are superposed with nightly mean values (crosses). Data points for which subtraction of sky and continuum resulted in a value of zero or less are shown with downward-pointing arrows, and these have been averaged into the nightly unweighted means as zeros. For one data set (triangles) taken after breakup (1 August), the instrument aperture was centered 100 arc sec from the nominal nucleus position along the tail (i.e., approximately the brightest location along the dispersed comet debris). This set showed gas productions about twice those measured at the nominal nucleus position; the dust "production" was larger by a factor of about 10. Only the 526-nm continuum data are plotted, because the $A(\theta)f\rho$ values at the other wavelengths show essentially the same behavior with distance. The vertical dotted line indicates the comet's distance at perihelion. The solid curve shown for CN is a quadratic fit to the mean values before breakup but excluding the 11 June outburst. This curve has been transposed to the other species (dashed curves), scaled to the 13 July mean value in each case. The other gas species generally match CN's trend with distance, but the essentially level trend of the dust production at large $r_H$ indicates that much of the dust is probably old material released at an earlier epoch.

the outburst and the associated coma features were produced by a piece of the nucleus breaking off and exposing a pocket of fresh ices to sunlight.

It is possible that the wings are produced by two separate jets on opposite sides of the nucleus. However, with two active regions, it is difficult to explain why the wings look so much alike from night to night and consistently appear concurrently with outbursts, not only in our images but also in those obtained by Tozzi and Licandro (*22*). Instead, we propose that both wings are produced by a single active area located 10° to 20° from the equator on a rotating nucleus (*23*). (Fortuitous timing of the 8 July image actually caught the vent near the plane of the sky, and the dust being emitted forms the 5000-km plume.) If this interpretation is correct, then the line of symmetry of the wings represents the projection of the spin axis onto the sky, allowing us to determine some of the fundamental properties of the nucleus. First, there is no change in projected position of the axis during the period 5 to 9 July, so there is no significant complex rotation on time scales of a few days. Next, we used images from the outburst of 3 to 4 June (which also exhibit axial symmetry) in conjunction with those from 5 to 9 July to estimate the orientation of the rotation axis in space (*24*): right ascension = 109°, declination = +22°, with an estimated 10° to 20° uncertainty and an unknown direction of rotation. The line of symmetry in the Tozzi and Licandro (*22*) image from 21 July is consistent with this orientation. Given this pole position, the axis, projected onto the sky, points toward the Sun in early July (although the actual subsolar latitude is around 50°). Thus, an active region near the equator would produce jets perpendicular to the comet-Sun line, which is not only consistent with the wing positions but also explains why the coma in the sunward direction changes little during the 5 July outburst. Finally, the uniformity of the two wings suggests that the rotation period of the nucleus is relatively short (<12 hours), with the material in opposing wings being replenished frequently to maintain the uniform appearance. If the rotation took half a day or more, then one wing would dissipate while the other is replenished, producing asymmetric wings.

There is significant evidence showing that outbursts were common in the 2 months before breakup. SWAN/SOHO measurements [assuming a phase lag of 1 to 2 days (*6, 25*)], combined with our and other data (*5, 17*), show that large outbursts began on 2 to 3 June, 16 to 17 June, 5 July, and 18 to 19 July, with smaller ones in between. Irregularities in the timing and size of these events suggest that they were initiated by a buildup of pressure as pockets of

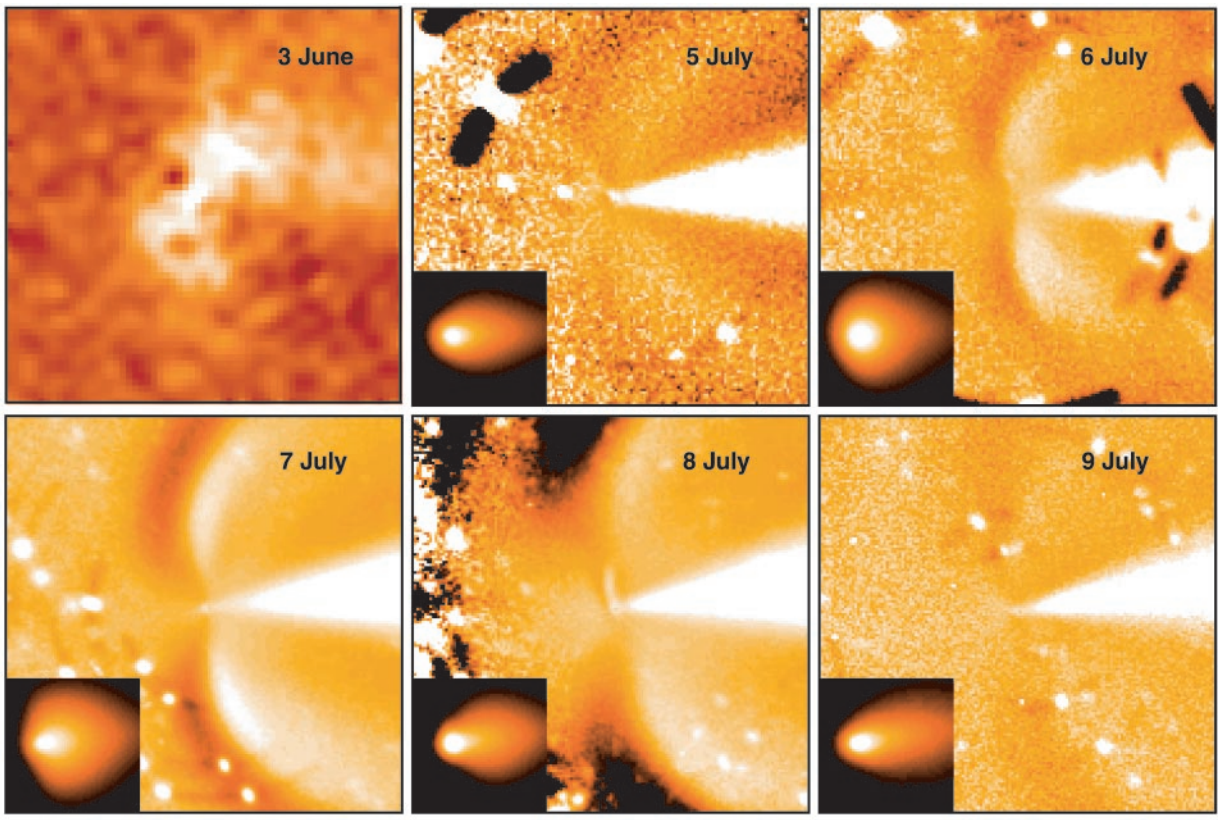


**Fig. 2.** Sequence of pseudocolor images showing the coma morphology on 3 June and around the time of the 5 July outburst. The images, obtained with the R band filter (120 nm wide, centered at 650 nm), have been processed by taking an average of the image as it is rotated through an angle of 45°, and then dividing the original by the averaged frame to remove the bright central peak and enhance radial features (*41*). Dark streaks bracketing the bright stars are an artifact of this processing technique. Other processing techniques reveal the same coma features, but with lower contrast than presented here. All images are oriented with celestial north at the top and east to the left, and have a field of view of $5 \times 10^4$ km. The small inset frames in the July images show, at the same scale, the shape of the inner third of the larger frame with no enhancement. For the June image, the Sun is located at a position angle (PA) of 96° (to the left) and is 61° out of the image plane; the rotation pole lies at a PA of 77° and extends into the image at an angle of 22°. For 7 July, the Sun is located at a PA of 95° and is about 13° out of the image plane; the rotation pole is positioned at a PA of 94° and extends into the image at an angle of 33°. The bright triangle to the right is the ion tail. Throughout the July sequence (both processed and unenhanced versions), "wings" can be seen forming perpendicular to the comet-Sun line, and then fading again. In the 8 July image, a plume of material at least 5000 km long can be seen, and it is likely that a jet, rotating with the nucleus, produced both the plume and the wings. In the inset frames, the central condensation becomes more elongated after the outburst, which is caused by debris, ejected during the outburst, moving down the tail. A similar morphology, although at lower resolution and rotated clockwise by about 20°, can be seen in the 3 June image, which was also obtained shortly after an outburst.

volatile ices were vaporized by heat from the Sun propagating into the nucleus.

After the breakup, we obtained eight nights of CCD observations at the Lowell and Perth observatories: from 26 July, shortly after the first outward signs of the breakup became apparent, through 10 August (Table 2). Figure 3 depicts a representative sample of the post-breakup morphology, showing the elongation of the central condensation [compare Kidger (*26*)], fading of the coma, and the dissipation of debris down the tail. Although the HST images show fragments 50 to 120 m in diameter (*5*), the spatial resolution of our images was insufficient to resolve any subnuclei. None of our images after breakup were obtained under photometric conditions, so we used a measure of the total integrated light in the tail on 4 August, given by Weaver *et al*. (*5*), to calibrate the surface brightness in our image on that night.

We quantified some characteristics of the comet remnants by using a Finson-Probstein (F-P) technique (*27, 28*) to model the dust released during the breakup. The properties determined or constrained in the F-P method are the particle size distribution (PSD) $f(a)$, dust production rate $\dot{N}(\tau)$, and dust emission velocity $v(a,\tau)$, where $a$ is the radius of the grain (μm) and $\tau$ is the time, measured relative to perihelion, that it was emitted. To minimize the number of free parameters, we adopted power laws to represent both $f(a)$ and $v(a)$. The best fit to all the images in the sequence was obtained by systematically varying the parameters (*29*).

From other measurements (*30*), we know that dust production had dropped to a negligible level a few days after the disruption, after which no significant new dust was added to the tail. This fact simplifies the modeling process, because only the motions of the existing dust need to be reproduced, without the difficulties that arise when new dust is added between different images. Unfortunately, the breakup also introduced a number of complications that are not accounted for in the F-P technique (*31*). To minimize the effect of these problems, we simply modeled the general shape and surface brightness of the tail, without attempting to match minor morphological features. We used images from 27 and 31 July and from 4 and 10 August to represent the post-breakup evolution of the tail (Fig. 3).

We began by modeling the 4 and 10 August images. Because radiation pressure has pushed the small grains out of these fields of view, the properties of the larger particles [$a$ = 30 to 300 μm (*32*)] can be more easily constrained. The model results indicate that the PSD of these larger grains varies as $a^{-2.4}$—more heavily weighted toward large particles than is the –3 to –4 size index seen in typical comets (*33, 34*), but not surprising because big particles are to be expected in a breakup. The velocity of the larger grains varied as $550a^{-0.55}$ m s$^{-1}$ in early July, but started dropping shortly before the breakup until, by the end of the breakup, it had fallen to one-third of its initial value ($\sim 200a^{-0.55}$ m s$^{-1}$). The model also shows two periods of increased dust production: one in early July (presumably the 5 July outburst) and another that began about 19 to 20 July (the start of the breakup). The levels of activity between these dates are masked by the massive quantity of dust produced in the breakup. From the shape and position of the brightest region in the tail on 10 August, with a sharp leading edge in the sunward direction, the model shows that large grain production peaked about 20 to 21 July and then decreased to a negligible level by 23 July. If a significant number of large grains were emitted after this time, then the leading edge would not drop off as fast as is observed.

Having determined the parameters for the large dust grains, we then modeled the 27 and

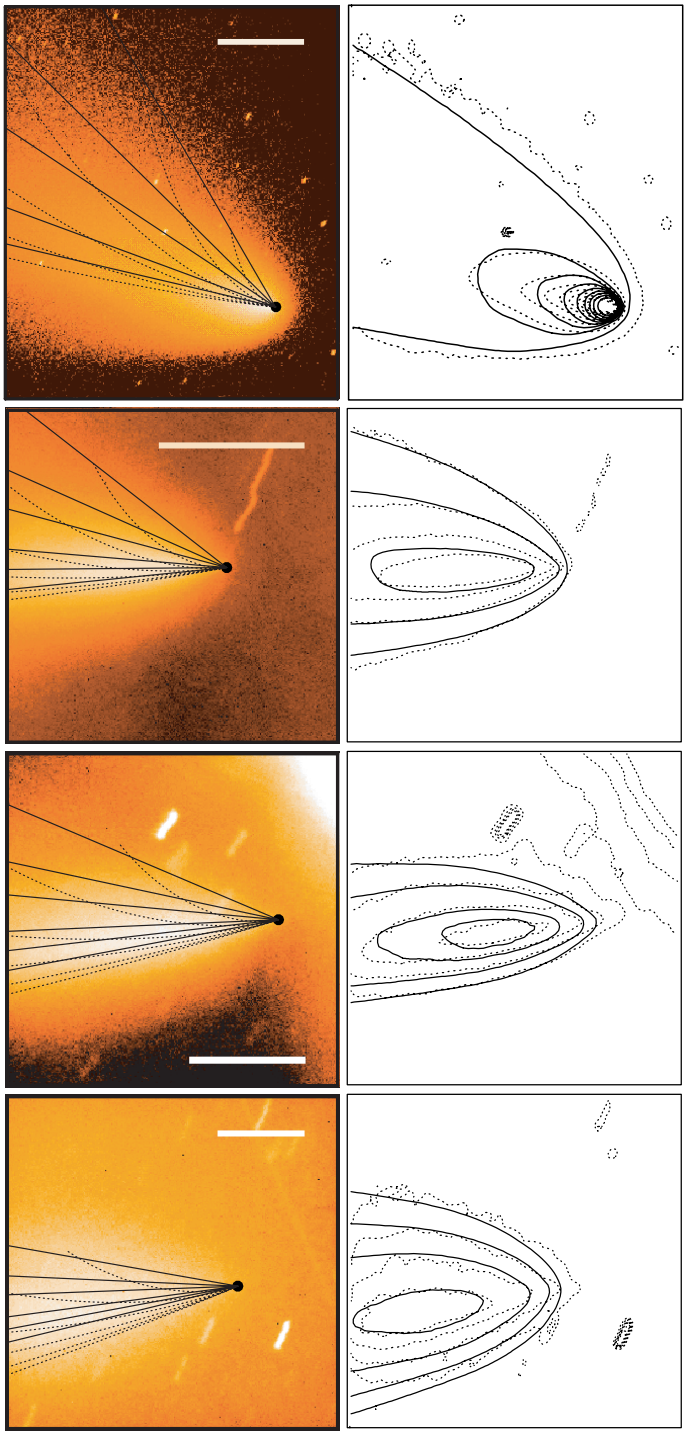

**Fig. 3.** Images and results from the dust tail modeling after the nucleus disintegrated. The left column displays the images used as input for the dust tail models, with syndynes and synchrones overlaid to map the basic tail structure. From top, images are from 27 and 31 July and from 4 and 10 August. They were obtained with a broadband R filter (*1*) and are oriented with celestial north at the top and east to the left. The streaks are background stars that have been smeared out because the telescope was tracking the comet's motion. (The squiggle seen on 31 July indicates poor tracking.) Scale bars are 5 × 10$^4$ km at the distance of the comet. Syndynes (dotted lines) are for particles of (clockwise from bottom) 1, 3, 10, 30, 100, and 300 μm. Synchrones (solid lines) represent emission times of (clockwise from bottom) 0, –5, –10, –20, –30, and –50 days relative to perihelion, except for 27 July, which does not include the 0-day synchrone. The right column displays the final model contours (solid) compared to the input image contours (dashed). The model results show that the breakup started around 19 July, with subfragmentation of the debris continuing for several days. Even before the breakup, the dust in the tail exhibited a PSD dominated by larger particles than are seen in more typical comets, although the emission velocities were not unusual.

31 July images where small particles ($a$ = 1 to 30 μm) dominate the surface brightness. Results from this analysis show a notable difference in production of large and small grains during the breakup. If we force the emission of small particles to mimic that of the larger ones (e.g., stopping by 23 July), then the coma is noticeably elongated by 22 July. Observations from this time, however, show that the coma did not elongate until after 24 July (*26, 35*), which means that small grain production must have continued for at least 2 days after large grain production ceased. Thus, the PSD changed during the course of the outburst, shifting toward smaller grains. We find the PSD for the small grains to be around $a^{-2.8}$, although it is not well constrained.

The peculiarities in the dust emission described above suggest that the ultimate breakup of C/LINEAR began around 19 to 20 July, with an abundance of large particles produced in the initial stages of the disintegration. Sublimation of the ices binding the larger particles together would then cause subfragmentation into smaller and smaller grains over the next few days, leading to an exponential increase in the exposed surface area, which in turn led to the final outburst. When the volatile ices were depleted, the outburst died out, leaving only small fragments and residual debris. The low dust velocities after the breakup support this scenario, because the smaller grains produced by fragmentation maintain the velocity of their larger, slower parent particle, rather than exhibiting the higher velocities of grains emitted directly from the nucleus. Furthermore, independent observations from other studies support 19 to 20 July as the start date of the disruption: Substantial increases in the production rates of HCN (*17*), neutral hydrogen (*6*), and dust [$A(\theta)f\rho$] (*22*) were all observed starting around 19 July and continuing for several days.

We can estimate the total mass seen in the tail by integrating over the particle masses in the model. If we assume a bulk density of 1000 kg m$^{-3}$ for the grains (*36*), the visible dust in the tail represents a mass of about $3 \times 10^8$ kg, which is comparable to one of the larger fragments in the HST images (*5*). Because numerous fragments were detected, it is clear that the visible dust in the tail represents only a small fraction of the original comet's mass. Furthermore, a significant amount of mass must be hidden in remnants between 1 mm and 50 m in diameter, which are too large to contribute significantly to the surface brightness of the tail (*32*) but are too small to be resolved in ground-based or HST images. In fact, our constraint on the original comet's radius (0.44 km) gives a mass of at least $4 \times 10^{11}$ kg, requiring that the vast majority of remnant material resides in the particles from 1 mm to 50 m (*37*) that we are not seeing.

Given this potentially extreme amount of hidden dust and the total ice mass of about $10^9$ kg computed by Bockelée-Morvan *et al.* (*17, 38*), it is clear that the original nucleus contained far more dust than ice. It is believed that ices act as the "glue" that binds the nucleus together, and if C/LINEAR started out with a relatively small amount of ice, then this would be a major factor in the ultimate disintegration. We also note that a dust-to-ice ratio of ~400 in this comet cannot be directly related to the typical ratios (~1) measured from the comae of other comets. In the case of C/LINEAR, all of the mass (ice and dust) was released during the breakup, whereas normal measurements from the coma are only sensitive to the dust particles small enough to be lifted off the surface by the gas flow; larger grains remain trapped on the nucleus. Thus, dust-to-ice ratio measurements from the coma are not necessarily representative of the nucleus as a whole.

The data suggest two mechanisms that could have led to the breakup. First, near perihelion, where sunlight is most intense, the rotation axis points toward the Sun and one hemisphere is almost exclusively exposed to sunlight. This continuous heating would allow a

**Table 2.** Summary of observational circumstances for CCD imaging observations. The listed UT dates are mid-times of the observations. The observing sites LO, MD, and PO refer to Lowell Observatory, McDonald Observatory, and Perth Observatory, respectively, and $r_H$ and $\Delta$ are the heliocentric and geocentric distances.

| UT date | Site | $r_H$ (AU) | $\Delta$ (AU) |
|---|---|---|---|
| | *1999* | | |
| 2.3 Nov | LO | 3.941 | 3.088 |
| 3.3 Nov | LO | 3.930 | 3.068 |
| 2.3 Dec | LO | 3.594 | 2.651 |
| 3.3 Dec | LO | 3.594 | 2.651 |
| | *2000* | | |
| 6.2 Jan | LO | 3.199 | 2.646 |
| 7.2 Jan | LO | 3.187 | 2.651 |
| 8.2 Jan | LO | 3.176 | 2.657 |
| 24.2 Jan | MD | 2.983 | 2.767 |
| 25.3 Jan | MD | 2.971 | 2.775 |
| 26.2 Jan | MD | 2.959 | 2.782 |
| 28.3 Jan | MD | 2.935 | 2.798 |
| 29.2 Jan | LO | 2.922 | 2.805 |
| 30.2 Jan | LO | 2.910 | 2.813 |
| 26.2 Feb | LO | 2.573 | 2.984 |
| 27.2 Feb | LO | 2.561 | 2.989 |
| 7.1 Mar | MD | 2.445 | 3.016 |
| 8.1 Mar | MD | 2.432 | 3.018 |
| 10.1 Mar | MD | 2.407 | 3.021 |
| 3.4 Jun | LO | 1.252 | 1.935 |
| 4.4 Jun | LO | 1.239 | 1.907 |
| 1.4 Jun | LO | 0.908 | 1.013 |
| 2.4 Jul | LO | 0.898 | 0.976 |
| 3.4 Jul | LO | 0.888 | 0.939 |
| 5.4 Jul | MD | 0.869 | 0.865 |
| 6.4 Jul | MD | 0.860 | 0.828 |
| 7.4 Jul | MD | 0.852 | 0.791 |
| 8.4 Jul | MD | 0.844 | 0.755 |
| 9.4 Jul | MD | 0.836 | 0.719 |
| 26.2 Jul | LO | 0.765 | 0.383 |
| 27.2 Jul | LO | 0.765 | 0.399 |
| 28.2 Jul | LO | 0.766 | 0.418 |
| 31.4 Jul | PO | 0.771 | 0.496 |
| 2.5 Aug | PO | 0.777 | 0.558 |
| 3.5 Aug | PO | 0.780 | 0.592 |
| 4.5 Aug | PO | 0.785 | 0.626 |
| 10.4 Aug | PO | 0.818 | 0.842 |

**Table 1.** Summary of photometry observations. The listed UT dates are mid-times of the observations, log ρ is the range of projected aperture radii measured each night, and θ is the phase angle of the comet (Sun-comet-Earth angle). The given production rates are nightly averages.

| UT date | $r_H$ (AU) | θ (°) | No. of obs. | log ρ (km) | log $Q$ (molecules s$^{-1}$) | | | | | log $A(\theta)f\rho$ | | | log $Q(H_2O)$ ($10^{26}$ mol s$^{-1}$) |
|---|---|---|---|---|---|---|---|---|---|---|---|---|---|
| | | | | | OH | NH | CN | $C_3$ | $C_2$ | λ3448 | λ4450 | λ5260 | |
| 5.3 Dec 1999 | 3.561 | 7 | 4 | 4.76–4.96 | 26.80 | — | 24.08 | — | — | 2.38 | 2.47 | 2.46 | 5 |
| 28.2 Dec 1999 | 3.297 | 14 | 3 | 4.76–4.95 | 26.68 | — | 24.22 | 24.01 | 24.03 | 2.35 | 2.24 | 2.30 | 4 |
| 30.2 Dec 1999 | 3.273 | 15 | 2 | 4.76 | — | — | 24.27 | 23.59 | 24.57 | 2.13 | 2.14 | 2.20 | — |
| 27.2 Jan 2000 | 2.939 | 20 | 3 | 4.51–4.72 | 27.19 | 25.49 | 24.56 | 23.63 | 24.05 | 1.89 | 2.23 | 2.40 | 12 |
| 25.2 Feb 2000 | 2.580 | 19 | 6 | 4.75 | — | — | 24.71 | — | — | — | 2.21 | 2.27 | — |
| 26.1 Mar 2000 | 2.192 | 13 | 1 | 4.54 | — | — | 24.93 | — | 24.55 | — | 2.41 | 2.26 | — |
| 27.1 Mar 2000 | 2.179 | 13 | 2 | 4.43 | — | — | 25.00 | — | 24.66 | — | 2.42 | 2.41 | — |
| 10.4 Jun 2000 | 1.152 | 36 | 3 | 4.67–4.76 | 28.37 | 25.87 | 25.50 | 24.30 | 25.27 | 2.82 | 2.81 | 2.85 | 295 |
| 11.4 Jun 2000 | 1.139 | 37 | 4 | 4.46–4.76 | 28.51 | 26.04 | 25.67 | 24.65 | 25.45 | 2.73 | 2.84 | 2.88 | 417 |
| 12.4 Jun 2000 | 1.126 | 38 | 4 | 4.65–5.07 | 28.38 | 25.93 | 25.49 | 24.07 | 25.27 | 2.76 | 2.76 | 2.82 | 309 |
| 13.4 Jul 2000 | 0.805 | 95 | 7 | 4.18–4.48 | 28.25 | 26.12 | 25.46 | 24.27 | 25.28 | 2.56 | 2.57 | 2.60 | 269 |
| 29.2 Jul 2000 | 0.768 | 108 | 1 | 4.20 | 27.35 | 25.47 | 24.41 | — | 24.15 | 1.35 | 1.47 | 1.58 | 35 |
| 30.2 Jul 2000 | 0.769 | 105 | 1 | 4.23 | — | — | — | — | — | — | — | 1.35 | — |
| 1.2 Aug 2000 | 0.774 | 98 | 2 | 4.28 | 27.27 | 25.12 | 23.96 | 23.43 | 23.85 | 1.64 | 1.08 | 1.02 | 19 |

strong thermal wave to propagate into the interior, where sublimation of volatiles could disrupt the nucleus. Second, a fragment breaking off the nucleus would expose fresh ices to the Sun. Explosive sublimation of these ices might then cause adjacent fragments to break off, revealing more fresh ice. Escalation of this process would lead to a runaway effect and the comet would simply unravel. The similarity in coma morphology during the various outbursts supports the latter mechanism. In the three events observed in detail, the coma features (e.g., the "wings") have about the same shape, suggesting that the activity driving the outburst originated at the same or an adjacent region on the nucleus in each case. This could signal the early stages of the unraveling process, leading up to the complete disruption on 23 July.

### References and Notes


1. Narrowband photometry was performed using the HB comet filters (*39*) to isolate flux from gas species and the underlying dust continuum. For CCD imaging, we typically used broadband V and R filters (554/85 nm and 650/120 nm, respectively), although when the comet was bright enough we also used the HB narrowband filters to investigate any structure present in the gas emission.
2. Gas production rates were computed using the standard Haser model and our nominal model scale lengths. $A(\theta)f\rho$ is a proxy for dust production, where $A(\theta)$ is the albedo at the particular phase angle of the solar illumination at the time of the observation, $f$ is the filling factor of the grains within the field of view of the photometer entrance aperture, and $\rho$ is the projected radius of the aperture. The quantity $A(\theta)f\rho$ is aperture-independent for dust having a canonical $1/\rho$ spatial distribution, and is independent of wavelength for grains that are gray in color.
3. As a result of very short observing windows and the associated high air mass for many of the observations from December to March, some species (OH, NH, $C_3$, and $\lambda$345 nm) were not always observed. Additionally, the relatively high dust-to-gas ratio seen early in the apparition, coupled with the low signal-to-noise ratio, resulted in low or negative gas fluxes after subtraction of the underlying continuum.
4. D. Schleicher, C. Eberhardy, *IAU Circular 7455* (2000).
5. H. A. Weaver *et al.*, *Science* **292**, 1329 (2001).
6. J. T. T. Mäkinen, J.-L. Bertaux, M. R. Combi, E. Quémerais, *Science* **292**, 1326 (2001).
7. The CN production rate curve was transposed to each of the other species by applying a simple scaling factor to the production rates based on the relative abundances measured in June and July.
8. A dynamically new comet is one having an orbit that is statistically likely to occur only upon the comet's initial return to the inner solar system from the outer Oort Cloud. Subsequent passages will be in modified orbits because of perturbations by the giant planets.
9. F. L. Whipple, *Moon Planets* **18**, 343 (1978).
10. M. F. A'Hearn, R. L. Millis, D. G. Schleicher, D. J. Osip, P. V. Birch, *Icarus* **118**, 223 (1995).
11. D. C. Jewitt, K. J. Meech, *Astrophys. J.* **310**, 937 (1986).
12. We used an empirical conversion to compute vectorial model water production rates from our Haser model OH production rates (*10*). We computed the minimum nucleus surface area using a water vaporization model (*40*), updated by A'Hearn *et al.* (*10*), and a geometric albedo of 5%. This technique implicitly assumes that none of the water comes from indirect sources such as icy grains, but given the consistency in the computed surface area for $1 < r_H < 3$ AU, we believe this is a valid assumption.
13. The baseline derived active area (excluding outbursts) from SWAN/SOHO (*6*) drops from about 1.3 km$^2$ in late May to 0.7 km$^2$ by 18 July. These areas are systematically lower than our values because of a combination of somewhat lower derived water production rates and differences between the water vaporization models.
14. Seasonal variations could also produce a decrease in activity; however, in this case, the effect goes in the wrong direction. Imaging data discussed below indicate that the Sun moved from near the equator toward the pole during this time, which would be expected to produce an increase in the total activity (*10*).
15. A. L. Cochran, W. D. Cochran, *Bull. Am. Astron. Soc.* **32**, 1070 (2000).
16. H. F. Levison, M. J. Duncan, *Icarus* **127**, 13 (1997).
17. D. Bockelée-Morvan *et al.*, *Science* **292**, 1339 (2001).
18. M. J. Mumma *et al.*, *Science* **292**, 1334 (2001).
19. When the comet was outside of solar conjunction, we have approximately monthly coverage. During the months of January and July, however, we have extensive observations.
20. The length of the plume is 5000 km as projected onto the plane of the sky. It could be longer if the jet points toward or away from Earth. This plume is discernible even in unprocessed images, so we are confident that it is not an artifact of the image enhancement.
21. We searched, unsuccessfully, for this fragment in our data. Estimates of the separation speed (*5*) indicate that even on 9 July, the fragment would be too close to the nucleus to be resolved in our images.
22. G. P. Tozzi, J. Licandro, in preparation.
23. If the spin axis lies near the plane of the sky, then throughout most of the rotation, the jet's emission is directed roughly toward or away from Earth, and no structure can be discerned. At two points during the rotation, however, the vent lies near the plane of the sky, and material emitted from the jet at these times is seen side-on. As this dust moves out from the nucleus and gets pushed away from the Sun by radiation pressure, it is seen as the wings.
24. For each date, the rotation axis is located in a plane defined by the line of sight and the projection of the rotation axis onto the sky (e.g., the line of symmetry). The intersection of planes from different dates is then used to determine the pole orientation in three dimensions.
25. The SWAN instrument on SOHO monitored the entire neutral hydrogen coma of C/LINEAR from late May to mid-August (*6*) and recorded a number of outbursts. The large size of the hydrogen coma introduces a significant phase lag (1 to 2 days) and dilution in amplitude of the observed peak in hydrogen abundances as compared to the instantaneous activity at the nucleus caused by an outburst.
26. M. Kidger, *IAU Circular 7467* (2000).
27. M. L. Finson, R. F. Probstein, *Astrophys. J.* **154**, 353 (1968).
28. The F-P technique uses the "sorting" effects of radiation pressure on different-sized grains to model the surface brightness of the dust tail. For any given date, it is possible to compute the location, relative to the nucleus, of a given particle radius $a$ emitted at an earlier time $\tau$. In accord with this concept, $a$ and $\tau$ are used to compute the positions of syndynes (the locus of particles of a single size emitted over a range of times) and synchrones (the locus of different-sized particles all emitted at a specific time), which map the distribution of grains in the tail. The expected surface brightness is computed by adding the contributions from all different dust sizes emitted over all times of interest. The particle size limits in the model are set by the information content of the images, and the amount of light reflected by each combination of $a$ and $\tau$ is determined by the model parameters outlined in the text.
29. Outward expansion of the dust after it leaves the nucleus causes the surface brightness contribution from one set of ($a$, $\tau$) values to overlap with that from other sets. Thus, a small change in one parameter can be offset by a change in another parameter, allowing multiple solutions to reproduce the tail profile in an image. For comets with widely spaced syndynes and synchrones (e.g., Fig. 3), this cross-parameter variation can be reduced to 5% or so, which is small enough to have no effect on the conclusions presented here. In addition, modeling a sequence of images introduces temporal constraints that reduce the cross-parameter variations even more.
30. Photometry after the breakup (Fig. 1) shows that the gas production dropped by at least a factor of 5, whereas the amount of dust was reduced by a factor of 10. Also, HST images (*5*) show that by 5 August, the large fragments were emitting a negligible amount of dust compared to that already in the tail.
31. Complications introduced by the breakup include numerous fragments emitting dust rather than a single source, a changing PSD resulting from fragmenting grains, and light from ion and gas species that cannot be separated from the light reflected by dust. Although we cannot tightly constrain the effects of these problems, we believe that they will not affect the parameters at a level of more than a few percent. In addition, their influence is most severe immediately after the disruption and diminishes with time. For example, the numerous large fragments are all very close together relative to the tail dimensions, so they mimic a single nucleus. By the time they have moved apart, their activity levels have also dropped significantly, as seen in the HST images (*5*). One problem that gets worse with time is that there is no well-defined nucleus to use as a reference point for the dust motions. We minimize this problem by modeling several images in a sequence, because constraints from the first image, where the nucleus is defined, will propagate through successive images.
32. Because there are many more small grains than large ones in a typical PSD, the light scattered from the small particles contributes most of the surface brightness of the tail. In our sequence of images, the light scattered by particles larger than 300 $\mu$m is completely overwhelmed by that from smaller grains, so we cannot constrain the properties of grains larger than 300 $\mu$m. However, there are likely to be significant numbers of these larger grains (up to 50 m in diameter) left over after the breakup, and they contain the vast majority of the mass in a PSD (e.g., a 1-cm particle has the same mass as $10^{12}$ 1-$\mu$m particles, but the ensemble of smaller grains scatters more than $10^4$ times as much light).
33. W. Waniak, *Icarus* **100**, 154 (1992).
34. M. Fulle, *Astron. Astrophys.* **276**, 582 (1993).
35. A. Kammerer, *Int. Comet Q.* **22**, 71 (2000).
36. Densities of both the nucleus and individual dust grains are dependent on the bulk density of the material forming them, combined with how tightly that material is packed. With no information to constrain the actual density, we assume 1000 kg m$^{-3}$ for all computations in this report, with the acknowledgment that this could be off by a factor of $\sim$2 in either direction.
37. An estimate of the hidden mass can be found by extrapolating the dust PSD to particles up to 10 m in radius. PSD indices as steep as $-3.5$ can produce enough mass to account for a 0.44-km nucleus. Therefore, the hidden mass computed for the PSD index ($-2.4$) found for 30- to 300-$\mu$m grains in our model is sufficient to produce a parent body even larger than 0.44 km.
38. In our analysis, we assume that all of the ice in the nucleus was exhausted during the breakup. The fact that very little water production was measured after the breakup supports this assumption.
39. T. L. Farnham, D. G. Schleicher, M. F. A'Hearn, *Icarus* **180**, 147 (2000).
40. J. J. Cowan, M. F. A'Hearn, *Moon Planets* **21**, 155 (1979).
41. Application of this processing technique was slightly different for the two dates. The July images were rotated directly around the nucleus, whereas the June image was unwrapped in ($r$,$\theta$) space, shifted in the $\theta$ axis, and then rewrapped into the ($x$,$y$) image. The only difference between these applications is that the innermost two or three pixels of the June image are more sharply enhanced.


42. We thank the authors of the other reports in this special C/LINEAR edition, in particular H. Weaver, M. Combi, C. Lisse, and D. Bockelée-Morvan, for discussions that were useful in incorporating the different data sets into a cohesive picture. Supported by NASA grants NAG5-4384, NAG5-7947, and NAG5-9009 and by NSF grant NSF 9988007.

9 January 2001; accepted 11 April 2001